Astronomy & Astrophysics manuscript no. output
September 11, 2026
©ESO 2026

Torsionally excited methanol in massive young stellar objects: The role of the mid-IR radiation field.

C. Sanna[1,2], S. Leurini[2], A. Giannetti[3], E. Schisano[4], L. Testi[5,6], S. Molinari[4], J. S. Urquhart[7], T. Pillai[8], F. Massi[6], K. Immer[9], E. Molinari[10], and S. Casu[2]

[1] Dipartimento di Fisica, Università degli Studi di Cagliari, S.P.Monserrato-Sestu km 0,700, I-09042 Monserrato (CA), Italy
[2] INAF - Osservatorio Astronomico di Cagliari, Via della Scienza 5, I-09047 Selargius (CA), Italy
[3] INAF - Istituto di Radioastronomia di Bologna, Via Gobetti 101, 40129 Bologna, Italy
[4] INAF - Istituto di Astrofisica e Planetologia Spaziali, Via Fosso del Cavaliere 100, I-00133, Rome, Italy
[5] Alma Mater Studiorum – Università di Bologna, Dipartimento di Fisica e Astronomia "Augusto Righi", Via Gobetti 93/2, I-40129, Bologna, Italy
[6] INAF-Osservatorio Astrofisico di Arcetri, Largo E. Fermi 5, I-50125 Firenze, Italy
[7] Centre for Astrophysics and Planetary Science, University of Kent, Canterbury, CT2 7NH, UK
[8] Haystack Observatory, Massachusetts Institute of Technology, 99 Millstone Road, Westford, MA 01886, USA
[9] European Southern Observatory, Karl-Schwarzschild-Straße 2, 85748 Garching bei München, Germany
[10] Osservatorio Astronomico di Brera, Via Brera 28, I–20121, Milano, Italy

September 11, 2026

ABSTRACT

Context. Observing the earliest stages of high-mass star formation in the mid-infrared (mid-IR) is challenging because the extinction is high and the resolution limited. Millimeter vibrationally and torsionally excited transitions of several molecules have been proposed as indirect probes of local mid-IR radiation fields around young stellar objects (YSOs).
Aims. We investigate the excitation and spatial distribution of torsionally excited methanol (CH_3OH) in 12 high-mass star-forming clumps in different evolutionary stages, assessing their potential as tracers of the mid-IR luminosity of embedded protostars.
Methods. We analyzed rotational transitions of methanol within the same torsionally excited states $v_t \geq 1$ in the Atacama Large Millimeter/submillimeter Array (ALMA) 890 μm observations and compared them with Spitzer 24 μm data by plotting line luminosities normalized by methanol abundance against mid-IR luminosities.
Results. The torsionally excited methanol emission is generally compact and systematically coincident with ALMA dust continuum peaks and 24 μm emission, even in faint sources. The only clump without an IR counterpart also shows no $v_t \geq 1$ emission, supporting radiative pumping as the dominant excitation mechanism. We found a promising power-law trend between $v_t \geq 1$ methanol lines and 24 μm luminosities, largely independent of the methanol abundance.
Conclusions. CH_3OH $v_t \geq 1$ transitions appear to be promising tracers of local mid-IR radiation fields of embedded protostars, providing core-scale information even in highly extincted regions. As a pilot study, our results suggest that extending our study to a larger statistical sample is crucial for testing and improving this method.

Key words. Stars: formation – Stars: massive – ISM: molecules – ISM: lines and bands – Submillimeter: ISM – Infrared: stars

1. Introduction

High-mass stars ($M \geq 8M_\odot$) play a fundamental role in the evolution of galaxies. Through intense radiative and mechanical feedback, they profoundly affect their environment, regulating the energy balance and chemical composition of the interstellar medium and thereby affecting the entire star formation process (e.g., McKee & Ostriker 2007; Kennicutt & Evans 2012; Krumholz 2014). Despite substantial progress over the past decades (e.g., Zinnecker & Yorke 2007; Tan et al. 2014; Motte et al. 2018; Beuther et al. 2025), several fundamental stages, especially the earliest ones, in the formation of high-mass stars remain unclear. This is primarily due to a combination of observational challenges, including their short lifetimes, large distances, and their formation within dense, clustered, and highly obscured regions.

A major challenge in high mass star formation (HMSF) studies is the lack of robust observational diagnostics to classify young stellar objects (YSOs) according to their evolutionary stage. Although low-mass YSOs classification schemes are well established (e.g., Lada et al. 1984; André et al. 1993; Evans et al. 2009; Robitaille et al. 2006), their application to high-mass YSOs is complicated due to their deeply embedded and clustered nature (e.g., Zinnecker & Yorke 2007; Motte et al. 2018). Molinari et al. (2008) proposed to extend the use of $L_{\rm bol}/M_{\rm clump}$, the bolometric luminosity-to-envelope mass ratio (abbreviated as L/M), a commonly accepted evolutionary indicator in the low-mass regime (see Bontemps et al. 1996; Saraceno et al. 1996; André et al. 2000, 2008), to the high-mass regime as well. This ratio is expected to increase significantly over time, reflecting the rising central luminosity and the progressive dispersal of the surrounding envelope. The L/M diagram has frequently been used in large-scale surveys (e.g., Elia et al. 2010; Ma et al. 2013; Molinari et al. 2016; Elia et al. 2017; König et al. 2017; Giannetti et al. 2017; Urquhart et al. 2014, 2018; Molinari et al. 2025), supporting its validity as a proxy for identifying the evolutionary stages of massive protostars. Giannetti et al. (2017) further validated this

Article published by EDP Sciences, to be cited as https://doi.org/10.1051/0004-6361/202660283

trend using spectroscopic observations on a sample of selected sources from the APEX[1] Telescope Large Area Survey of the Galaxy (ATLASGAL; Schuller et al. 2009; Urquhart et al. 2018; Giannetti et al. 2014).

Although L/M is a widely accepted evolutionary indicator in the HMSF regime, it mainly reflects properties on large spatial scales. The bolometric luminosity, derived from spectral energy distributions (SED) of clustered regions, includes all radiation emitted by the sources. Even for deeply embedded early-stage objects that are often invisible in the mid-IR due to severe extinction, the reprocessed radiation emitted in the range from far-IR to (sub-)millimeter still makes L/M an effective indicator. However, $L_{\rm bol}$ is mainly derived from Herschel Space Observatory data (Pilbratt et al. 2010), which have a limited angular resolution. As a result, L/M typically traces clump-scale structures (~1–10 pc; e.g., Motte et al. 2018, 2022), reflecting the global emission budget of entire protoclusters. Currently, no IR facilities can directly trace the evolutionary stages of deeply embedded cores on the typical small scale (~0.01–0.1 pc; e.g., Motte et al. 2018, 2022). In recent decades, new telescopes have significantly improved the angular resolution, but much remains to be understood. For example, the James Webb Space Telescope (JWST; McElwain et al. 2023) provides a higher resolution in the near- and mid-IR, but it cannot fully overcome the challenges of extinction or sensitivity limitations.

We explore an alternative diagnostic: we use rotational transitions of methanol (CH_3OH) within the same torsionally excited states ($v_t \geq 1$) as indirect tracers of the mid-IR radiation field around individual high-mass YSOs. Our approach is based on the study of Carroll & Goldsmith (1981) on the radiative pumping of vibrational transitions of molecules via IR radiation. They were the first to describe that while rotational levels of the vibrational ground state can be populated by collisions and radiation for the CS molecule, the levels of the vibrational excited states are mainly populated by IR radiation. Infrared pumping has also been proposed for other molecules, including HC_3N (Goldsmith et al. 1982) and CH_3CN (Goldsmith et al. 1983). Since this mechanism indirectly links the intensity of these transitions to the IR radiation field of the background source, vibrationally excited transitions have been increasingly used as tracers of deeply obscured IR emission, such as from HC_3N in star-forming regions (e.g., Wyrowski et al. 1999; Chen et al. 2025), and from HCN in luminous galaxies (Aalto et al. 2015).

Menten et al. (1986) were the first to suggest that torsionally excited levels of methanol could also be radiatively excited by IR radiation. The same mechanism drives Class II CH_3OH maser emission (Sobolev & Deguchi 1994). Non-local thermal equilibrium (Non-LTE) radiative transfer modeling from Leurini et al. (2007b) confirmed that torsionally excited levels are radiatively populated by far-IR photons from the surrounding dust, while collisional excitation plays a negligible role under typical protostellar conditions. Empirical evidence further corroborated this theoretical framework. Giannetti et al. (2017) found a close correlation between the temperature derived from CH_3OH $v_t \geq 1$ lines and the 22 μm luminosity of massive clumps, indicating that these transitions are sensitive to the embedded IR radiation field. However, this correlation reflects integrated clump-scale properties, and further investigation at the core scale is essential to understand the relation between the radiation field and CH_3OH $v_t \geq 1$ lines in individual YSOs.

We investigate CH_3OH $v_t \geq 1$ lines as tracers of mid-IR radiation in individual YSOs, focusing on the core scale. Methanol is particularly well suited for this purpose because its $v_t \geq 1$ transitions are numerous within a narrow spectral range. This enables the simultaneous observation of multiple lines that are each potentially sensitive to photons of different mid-IR wavelengths and at high angular resolution. To assess the reliability of these transitions as proxies for the IR radiation, we compare their emission with the available 22–24 μm IR fluxes from YSOs in protoclusters in different evolutionary stages. We also explore correlations between line intensities in various excitation regimes and IR fluxes to evaluate the diagnostic potential of these transitions for probing the intensity of the local radiation field.

This paper is organized as follows. Sect. 2 describes the transitions and sample selection, observations, and data reduction. Sect. 3 presents the morphology of the Atacama Large Millimeter/submillimeter Array (ALMA) continuum emission in the observed protoclusters and the detection of torsionally excited methanol lines. In Sect. 4 we describe the analysis of the spatial distribution and the luminosity correlation between CH_3OH $v_t \geq 1$ transitions and mid-IR emission. The implications for the evolutionary classification and the potential of torsionally excited transitions as diagnostic tools are discussed in Sect. 5. Finally, we summarize in Sect. 6 our main results and discuss the prospects for future work.

2. Observations

2.1. Line selection

We selected torsionally excited transitions of methanol, specifically, the $7_k - 6_k$ band in the vibrational states v_t=1,2 (see the list of transitions in the Appendix Table B.1). The transition frequencies and spectroscopic parameters were obtained from the Splatalogue[2] database, which provides accurate line lists for ground and torsionally excited states.

The targeted transitions fall within the ~336.6–338 GHz spectral window and include a dense set of lines with upper-energy levels $E_u/k_B \simeq 350$–1000 K. These transitions were chosen because the energy gaps between the torsionally excited levels and the ground state correspond to photons in the ~14–40 μm range, consistent with the typical mid-IR emission of embedded protostars. As a result, these transitions serve as sensitive tracers of local mid-IR radiation near the source.

2.2. Sample selection

We selected clumps from the ATLASGAL[3] TOP100 sample (hereafter TOP100) (Giannetti et al. 2014), which includes approximately 110 massive clumps covering the full evolutionary sequence of high-mass star formation. Based on the classification scheme originally introduced by Giannetti et al. (2014) and Csengeri et al. (2016), König et al. (2017) refined it into four evolutionary stages: 70 μm weak, mid-IR weak, mid-IR bright, and H II regions, using 70 μm data from Herschel Infrared Galactic Plane Survey (Hi-GAL; Molinari et al. 2010),

[1] 12 m Atacama Pathfinder Experiment (APEX) telescope (Güsten et al. 2006).

[2] The Splatalogue Database for Astronomical Spectroscopy (`http://www.splatalogue.net/`) (Remijan et al. 2007), from which we selected entries from the Cologne Database for Molecular Spectroscopy (CDMS, Müller et al. 2001, 2005) and the Jet Propulsion Laboratory catalog (JPL, Pickett et al. 1998).

[3] ATLASGAL compact source catalogs are based on Contreras et al. (2013); Urquhart et al. (2014); Csengeri et al. (2014).

mid-IR emission at 21–24 μm from the Midcourse Space Experiment (MSX; Price et al. 2001), the Wide-Field Infrared Survey Explorer (WISE; Wright et al. 2010), and the Multiband Infrared Photometer for Spitzer survey of the inner Galactic Plane (MIPSGAL; Carey et al. 2009) with flux thresholds and radio-continuum observations at 4–8 GHz from the Coordinated Radio "N" Infrared Survey for High-mass star formation (CORNISH; Hoare et al. 2012; Purcell et al. 2013; Urquhart et al. 2013) and the Red MSX Source (RMS; Urquhart et al. 2007, 2009) surveys, complemented by targeted methanol maser observations (Walsh et al. 1999). The TOP100 sample is designed to include the brightest representatives of each evolutionary class in the ATLASGAL catalog (Contreras et al. 2013; Urquhart et al. 2014; Csengeri et al. 2014). Consequently, these clumps are among the best-characterized high-mass regions in the Galaxy through the extensive follow-up observations (e.g., Csengeri et al. 2016; König et al. 2017; Giannetti et al. 2017; Wienen et al. 2021; Billington et al. 2019).

This scheme was further refined by Urquhart et al. (2018, 2022), who classified sources as quiescent, protostellar, YSO, and H II regions. A key improvement over previous methods was that the arbitrary 24 μm flux threshold was replaced with the presence or absence of an 8 μm point source to distinguish protostellar objects from YSOs. This approach overcomes the limitations of fixed flux thresholds and provides a more comprehensive view in different wavelengths, including 3–8 μm from the Galactic Legacy Infrared Mid-Plane Survey Extraordinaire (GLIMPSE; Benjamin et al. 2003; Churchwell et al. 2009), 24 μm MIPSGAL, and 70 μm Hi-GAL images. We adopted the Urquhart et al. (2022) classification.

In Table 1 we present the 12 sources we analyzed, selected from the TOP100 sample. As a small subset, they inherit the well-characterized properties of the TOP100, making them an ideal starting point for a detailed study that spans all evolutionary stages. The TOP100 clumps were selected according to the following criteria:

1. Coverage of the full evolutionary sequence.
2. Distances ($d_{\rm ref}$) in the range 3–5 kpc (from Giannetti et al. 2014; Urquhart et al. 2022), which, given a typical ALMA angular resolution of ~0.5″, correspond to spatial resolutions of ~1500–2500 au. This is comparable to the typical sizes of dense protostellar cores (see Motte et al. 2007; Russeil et al. 2010; Motte et al. 2018; Coletta et al. 2025).
3. Clump masses ($M_{\rm clump}$) in the range 800–2000 $M_\odot$ (from König et al. 2017).
4. H_2 column densities ($N_{\rm H_2}$) in the range $(8–30)\times10^{22}$ cm^{-2} (from König et al. 2017), excluding too low column densities to optimize the detections and too high values for optical depth issues.

These criteria ensured a representative subset that covered all evolutionary stages of star formation while maintaining homogeneity within each class. After filtering the TOP100 sample according to these criteria, we initially identified 16 sources with an overabundance of H II regions. To preserve class homogeneity and for observational considerations, the selection was limited to 12 sources, restricting the number of H II regions, so that no class dominated the sample. The final distribution of sources is two quiescent sources, three protostellar sources, three YSOs, and four H II sources. In addition, nine of the sources in our subset were previously detected in torsionally excited methanol transitions by Giannetti et al. (2017), who used the same lines as we did (see Sect. 2.1).

2.3. Observations and data reduction

2.3.1. ALMA observations

Our study is based on ALMA Band 7 observations (~338 GHz, ~0.89 mm) from project ID 2017.1.00377.S (PI: S. Leurini), carried out during Cycle 5 (2017–2018 session). The data were obtained in spectral line mode as single-pointing observations using the 12 m main array and the 7 m Atacama Compact Array (ACA), which were combined to recover compact and extended emission. The 12 m array observations were performed in the C-3 configuration with baselines of ~15–680 m, corresponding to a largest angular scale (LAS) of ~5″ and a synthesized beam of ~0.6″ × 0.4″. The ACA observations cover baselines of ~9–49 m, recovering spatial scales up to ~17–19″ with a synthesized beam of ~4.7″ × 2.7″. The resulting rms noise levels are ~0.1–0.7 mJy beam^{-1} for the 12 m data and ~10–20 mJy beam^{-1} for the ACA data. The spectral setup consisted of four ~1 GHz spectral windows covering 336.4–340.2 GHz with a spectral resolution of ~0.488 MHz (~0.86 km s^{-1}), providing full coverage of the CH_3OH $7_k - 6_k$ transitions in the torsional states $v_t = 0, 1, 2$.

2.3.2. ALMA data reduction and imaging

The data calibration and image processing were performed using the Common Astronomy Software Applications package (CASA[4]; McMullin et al. 2007; CASA Team et al. 2022). The initial calibration followed the standard ALMA pipeline procedures (CASA 5.1.1[5]), with additional manual flagging applied to correct antenna-specific errors. Subsequent data reduction steps were performed with CASA 6.4.1[6], which provides updated analysis tools.

First, we combined the 12 m and 7 m data to recover compact and extended emission. We combined the visibilities using CASA tasks (see ALMA tutorials[7]) such as `mstransform` and `concat` to ensure that the datasets were properly aligned and merged. A critical step in the reduction was the identification of line-free channels, which is essential for an accurate continuum subtraction, especially given the high line-density typically observed toward massive YSOs. To address this, we used the ALMA pipeline `find_continuum` task (Hunter et al. 2023), which analyzes the mean spectrum of a dirty cube (produced with `tclean`) to identify channels contaminated by spectral lines. This procedure produces a `cont.dat` file that lists the frequency ranges corresponding to line-free regions, which were then used for continuum subtraction. The continuum subtraction was then performed in the *uv* domain using the `uvcontsub` task, assuming a zeroth-order (constant) baseline fit. The data imaging was performed with the `tclean` task using Briggs weighting (`robust` = 0.5), producing continuum images in `mfs` mode and spectral cubes in cube mode. The final combined cubes have a typical synthesized beam of ~0.6–1″, a cell size of ~0.1–0.2″, a field of view of ~29″, and a channel width of ~0.448 MHz (~0.435 km s^{-1}).

While the data reduction process is generally robust, the measured fluxes can be slightly affected by systematic uncertainties that primarily arise from residual baseline contributions after continuum subtraction. In complex line spectra, blended

[4] `http://casa.nrao.edu`

[5] The pipeline version required for Cycle 5 is casa-release-5.1.1; see `https://almascience.eso.org/processing`.

[6] Documentation CASA tasks: `https://casadocs.readthedocs.io/en/v6.4.1`.

[7] `https://casaguides.nrao.edu/index.php/ALMA_Tutorials`

Table 1. Properties of the selected sources.

Name	ATLASGAL CSC name	Class	Position (ICRS) R.A. (J2000)	Dec. (J2000)	d_{ref} (kpc)	v_{LSR} (km s^{-1})	v_{ref} (km s^{-1})
G014.49	AGAL014.492−00.139	quiescent	18:17:22	−16:25:01	3.1	40.5	39.5
G030.89	AGAL030.893+00.139	quiescent	18:47:13	−01:45:07	4.9	105.3	107.4
G014.19	AGAL014.194−00.194	protostellar	18:16:58	−16:42:16	3.1	38.7	39.4
G008.68	AGAL008.684−00.367	protostellar	18:06:23	−21:37:10	4.4	35.6	41.5
G023.21	AGAL023.206−00.377	protostellar	18:34:54	−08:49:19	4.6	77.5	77.4
G335.78	AGAL335.789+00.174	YSO	16:29:47	−48:15:51	3.3	−50.5	−49.4
G019.88	AGAL019.882−00.534	YSO	18:29:14	−11:50:26	3.3	43.2	44.5
G337.92	AGAL337.916−00.477	YSO	16:41:10	−47:08:04	2.9	−40.6	−38.9
G305.21	AGAL305.209+00.206	H II	13:11:13	−62:34:38	4.0	−42.9	−41.6
G301.14	AGAL301.136−00.226	H II	12:35:35	−63:02:30	4.3	−39.6	−39.3
G337.40	AGAL337.406−00.402	H II	16:38:50	−47:27:59	3.0	−42.5	−40.2
G343.13	AGAL343.128−00.062	H II	16:58:17	−42:52:08	2.7	−31.5	−35.5

Notes. The columns list the name: short source name used in this work; the ATLASGAL CSC name: source names from Contreras et al. (2013); the evolutionary class, source velocities (v_{LSR}), and distances (d_{ref}) from Urquhart et al. (2022); v_{ref}: reference velocity derived in this work from the CH_3OH $7_{-1} - 6_{-1}$, A^-, v_t=1 line and used to convert the observed spectra from the sky frequency into the rest-frame frequency.

or broad lines can affect the baseline determination. To account for these factors, we adopted a conservative 10% uncertainty on the integrated fluxes, in agreement with the typical absolute flux calibration uncertainty of 5–10% for ALMA Band 7 (see, e.g., Remijan et al. 2019; Francis et al. 2020; Braatz 2020). We also examined the residuals in line-free channels after baseline fitting, which indicated that the uncertainties introduced by continuum subtraction are consistent with the adopted 10%.

2.4. Auxiliary infrared data

We obtained the IR data from the NASA/IPAC Infrared Science Archive (IRSA[8]; Alexov et al. 2005; Teplitz et al. 2018)). Specifically, we retrieved mid-IR Spitzer images at 24 μm from the MIPSGAL survey (MIPS, ~6″; Carey et al. 2009), at 22 μm from the WISE survey (W4, ~12″; Wright et al. 2010), and at 8 μm from the GLIMPSE survey (IRAC, ~2″; Benjamin et al. 2003; Churchwell et al. 2009).

3. Observational results

3.1. Continuum emission

The ALMA 890 μm continuum maps for the 12 clumps in our sample are shown in Figs. 1 (for the younger sources) and 2 (for the most evolved clumps). The sample exhibits a broad range of continuum morphologies, reflecting different degrees of fragmentation and structural complexity. The youngest clumps in our sample, classified as quiescent (e.g., G014.49, G030.89), tend to show significant fragmentation, with multiple cores often distributed along filamentary structures. The clumps classified as protostellar and YSO show a broader variety of core distributions. Some (e.g., G023.21, G305.21) contain multiple compact cores embedded in clumpy or centrally concentrated structures, while others (e.g., G019.88, G337.92) display more elongated and irregular filamentary morphologies. In contrast, clumps classified as H II (e.g., G337.40, G301.14) generally present diffuse and more irregular continuum emission.

To characterize these structures, we identified dense cores using the 890 μm thermal dust continuum emission. The core positions were determined using the algorithm `dendrogram` (Rosolowsky et al. 2008), implemented in the package `astrodendro`[9] (Robitaille et al. 2019). The algorithm was applied to maps without primary beam correction to preserve a uniform noise level across the entire field. We explored different combinations of dendrogram parameters and adopted `min_value` = 5σ, `min_delta` = 1σ, and `min_npix` ≃ 18 pixels (approximately half of the synthesized beam area). The dendrogram algorithm segmented the emission into a hierarchical structure, with the smallest independent structure identified as leaves, which we considered to be dense cores. A leaf is detected when it consists of at least a minimum number of connected pixels (`min_npix`) above a fixed intensity threshold (`min_value`). Therefore, `min_npix` is a segmentation parameter that defines the smallest area required to identify a leaf and does not represent the minimum size of a physical source. For compact sources, the combination of a narrow emission profile and the adopted segmentation thresholds can result in a recovered area smaller than the synthesized beam area, especially for compact faint sources close to the detection limit or in crowded regions, as discussed by Rigby et al. (2024). Consequently, adopting a more conservative criterion, such as `min_npix` equal to one synthesized beam area, can lead to the exclusion of significant compact detections. Similar considerations motivated the adoption of comparable parameters in previous analogous studies (e.g., Hatchfield et al. 2020; Rigby et al. 2024; Wallace et al. 2026).

After the core identification, we measured the fluxes in the primary-beam-corrected maps to account for the antenna response. The fragmentation level in the 12 clumps is moderate, with approximately 3–11 cores per region, and all sources contain at least several detected cores. A summary of the number of cores identified in each region is given in Table 2.

We focused on the analysis of the torsionally excited methanol lines and only considered the cores in which these lines are detected. A detailed study of the continuum properties and core characteristics will be presented in a forthcoming paper.

3.2. Emission of CH_3OH v_t=1,2 rotational transitions

The spectra were extracted by integrating the ALMA data cubes over the areas of the dust continuum cores identified in Sect. 3.1. Since the spectral axis of ALMA cubes is provided in sky fre-

[8] `https://irsa.ipac.caltech.edu/frontpage/`

[9] `https://dendrograms.readthedocs.io/en/stable/`

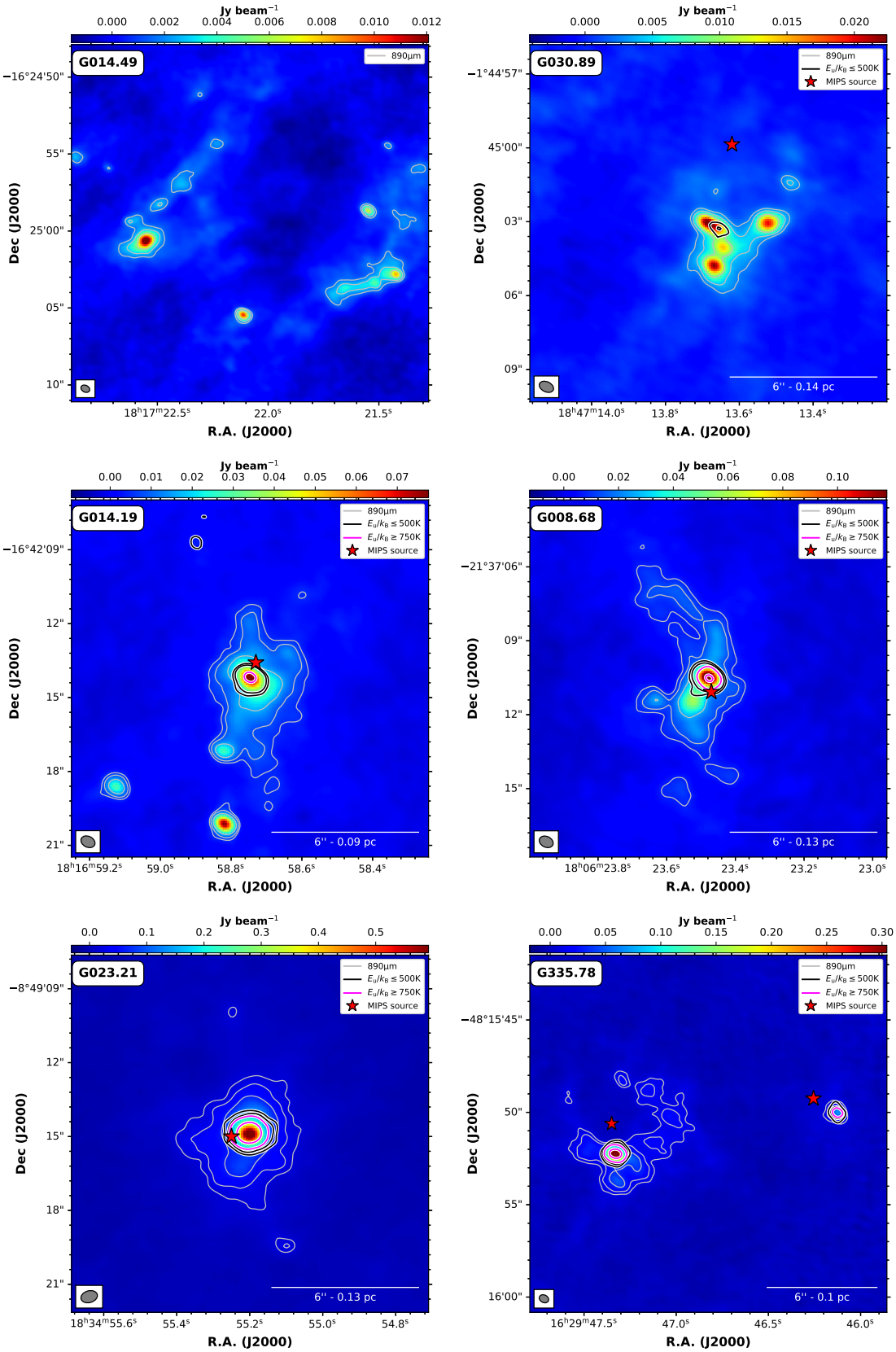

Fig. 1. ALMA 890 μm continuum images (background) of the younger clumps in the sample. The silver contours show the continuum emission at [3, 5, 10] σ. The black contours trace low-$\Delta E/k_B$ emission at [3, 5] σ, and the magenta contours indicate high-$\Delta E/k_B$ emission at [10, 50] σ. The red star marks point sources from the MIPSGAL catalog (Gutermuth & Heyer 2015), with exceptions for G030.89, and secondary sources in G335.78, where centroids are determined in this work. For G014.49, the absence of line contours and IR emission indicates a non-detection. The ALMA beam size (~0.6″) is shown in the bottom left corner, and the MIPSGAL (~6″) beam size is shown in the bottom right corner.

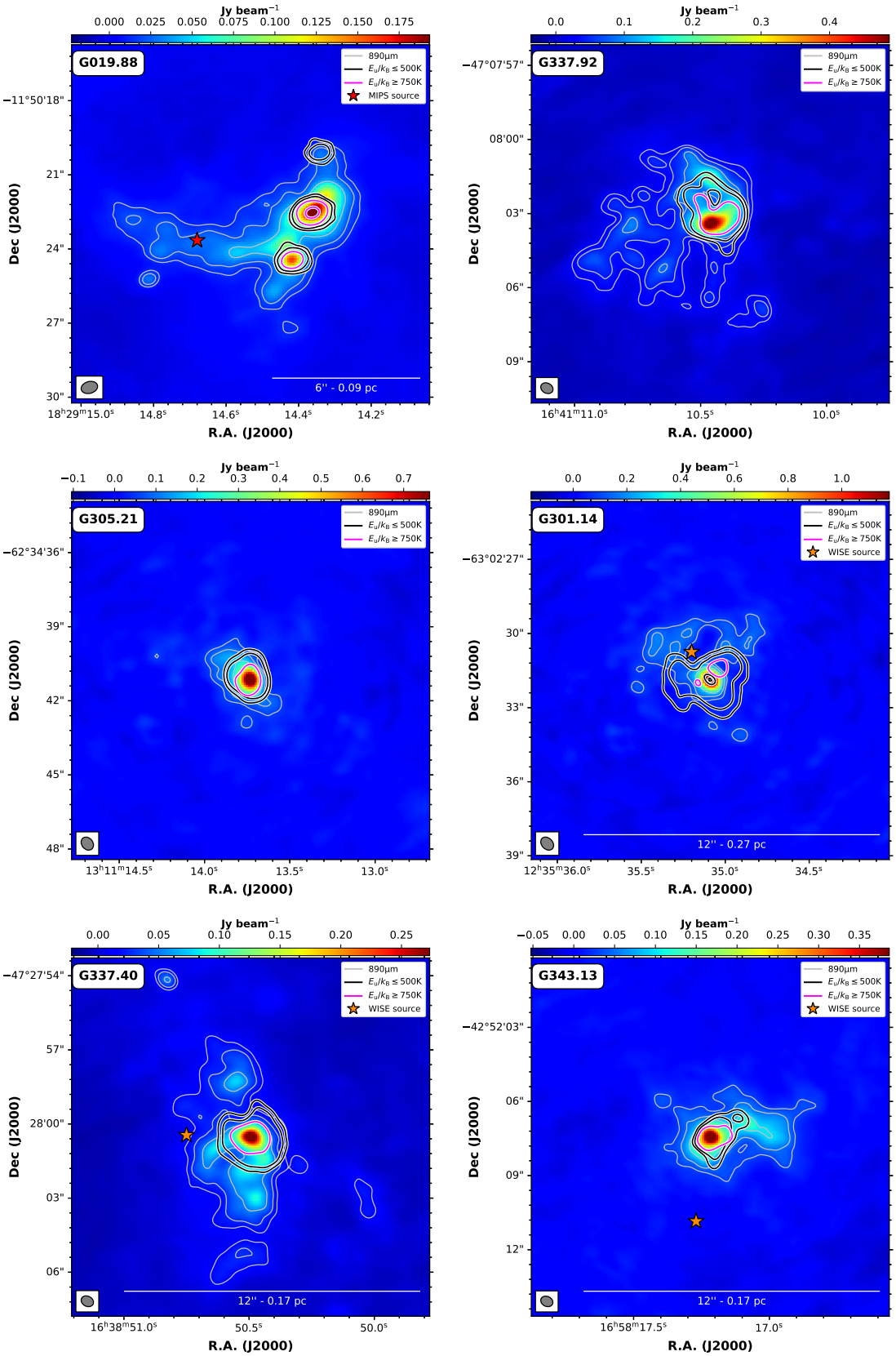

Fig. 2. ALMA 890 μm continuum images (background) of the evolved clumps in the sample. The silver contours show the continuum emission at [3, 5, 10] σ. The black contours trace low-$\Delta E/k_B$ emission at [3, 5] σ, and the magenta contours indicate high-$\Delta E/k_B$ emission at [10, 50] σ. All sources are saturated at 24 μm, except for G019.88, where the red star marks point sources from the MIPSGAL catalog (Gutermuth & Heyer 2015). The orange star indicates the centroid of the WISE catalog (Cutri et al. 2012) for G337.92, G301.14, G337.40, and G343.13. Absence of stars (e.g., G305.21, G337.92) indicates complex diffuse emission not in the catalogs. The ALMA beam size (~0.6″) is shown in the bottom left corner, and the MIPSGAL (~6″) or WISE (~12″) beam size is shown in the bottom right corner.

Table 2. Number of continuum cores identified via the dendrogram analysis at 5σ (see details in Sect. 3.1).

quiescent Clump	N. cores	protostellar Clump	N. cores	YSO Clump	N. cores	H II Clump	N. cores
G014.49	10	G014.19	8	G335.78	10	G305.21	6
G030.89	7	G008.68	7	G019.88	9	G343.13	3
		G023.21	3	G337.92	11	G301.14	8
						G337.40	7

quency, an accurate reference velocity is required to convert the spectra into the rest frequency and to reliably identify molecular lines. The systemic velocities reported for ATLASGAL clumps, derived from single-dish observations (e.g., Urquhart et al. 2022; Wienen et al. 2015), trace the integrated emission of various extended components of the gas envelope and can therefore be inadequate to represent the kinematics at the compact core scale. For this reason, we adopted the transition CH_3OH $7_{-1} - 6_{-1}$, A v_t=1 at 337.969438 GHz as a reference velocity (v_{ref}). This line was selected because it is relatively isolated compared to the other lines of the band, has a moderate upper-energy level for a v_t=1 transition ($E_u/k_B \simeq 390$ K), and is consistently detected in all sources with significant torsionally excited methanol emission, making it a reliable local velocity reference.

The spectral range covered by our observations contains a high density of molecular transitions, as noted in previous studies using similar observational setups (e.g., Sánchez-Monge et al. 2014; Beltrán et al. 2014). In particular, the interval between 336.6 and 339 GHz contains not only CH_3OH, but also several complex organic molecules (e.g., C_2H_5OH, CH_3OCH_3, and CH_3COOH) and other important species such as $C^{17}O$, SO_2, $C^{34}S$, and HC_3N. This spectral complexity complicates the flux determination of individual torsionally excited features and the baseline determination and introduces residual uncertainties in the measured fluxes that must be considered (see Sect. 2.3.1).

Fig. 3 shows representative spectra we analyzed, focusing on the CH_3OH $7_k - 6_k$ v_t=1,2 transitions, including approximately 40 lines in the narrow frequency range of ~336.6–338 GHz. Most transitions cluster in two main spectral windows: one window around ~337.6 GHz, and another window around ~337.2 GHz, corresponding to v_t=1 and 2, respectively. The most prominent feature appears at ~337.643 GHz, resulting from the blend of four v_t=1 transitions (k=0,1,−4,−5). This blended line is mainly dominated by transitions with $E_u/k_B \simeq 360$ K and consistently appears as the brightest feature due to the efficient excitation of its relatively low-energy levels (which are more easily populated) and the convolution of multiple transitions, which enhances the overall signal-to-noise ratio, thereby facilitating detection.

The line intensities vary significantly in the clumps and individual cores, reflecting differences in the physical conditions of each source. Overall, the line morphology is dominated by compact emission, with brighter emission generally associated with the more evolved objects. The linewidths (full width at half maximum, FWHM) typically range from ~4 to 10 km s^{-1}, and comparisons between transitions often reveal velocity gradients within or between individual cores.

Given the large number of torsionally excited lines, we first identified specific frequency intervals dominated by $v_t \geq 1$ transitions that were only marginally affected by contamination from other species. Since the CH_3OH $v_t \geq 1$ levels are considered to be predominantly populated by IR radiative pumping (e.g., Menten et al. 1986; Leurini et al. 2007b), we grouped the lines according to their upper-energy levels (E_u/k_B) to explore possible trends as a function of excitation energy. Using the relation $E = h\nu = hc/\lambda$, we associated each upper-energy level with a characteristic mid-IR wavelength. Although this correspondence cannot be interpreted as a direct identification of the exciting pumping photons, it provides a useful empirical proxy to investigate the role of the mid-IR radiation field in the excitation. The complete set of transitions spans a broad range of E_u/k_B, roughly corresponding to mid-IR wavelengths between ~ 14 and 40 μm, sampling an essential portion of the mid-IR SED. We divided the transitions into three empirical energy intervals ($\Delta E/k_B$): low (356–500 K), mid (500–750 K), and high (≥750 K), corresponding approximately to wavelength ranges of 29–40 μm, 19–27 μm, and 14–19 μm, respectively. These intervals were only chosen to sample different portions of the excitation range and should not be interpreted as distinct physical pumping regimes. These intervals were used to produce integrated moment-0 maps and compute the line luminosities presented in the following sections, excluding lines potentially contaminated by $C^{17}O$ (3 – 2) and ^{34}SO ($8_8 - 7_7$) (see Fig. 3).

We applied a 3σ threshold to each $\Delta E/k_B$. For the following analysis, only continuum cores with positive low-$\Delta E/k_B$ detection were considered. The results are summarized in Table 3. The source G014.49 in the sample alone lacks detectable $v_t \geq 1$ emission for any of its cores, and all other clumps exhibit $v_t \geq 1$ lines in at least one core. Typically, only one core per clump shows detectable $v_t \geq 1$ emission, but in some cases, multiple cores are detected: two cores in G335.78, G337.92, G301.14, and G343.13, and three cores in G019.88.

Figure 3 shows a portion of the observed spectrum for a representative subsample of cores showing the progressive detection of $v_t \geq 1$ transitions across different $\Delta E/k_B$ selected to cover a range of evolutionary stages. The sequence begins with G030.89 MM1 (classified as quiescent), which only shows low-$\Delta E/k_B$ emission. In contrast, G019.88 MM3 exhibits low- and mid-$\Delta E/k_B$ emission, but lacks high-$\Delta E/k_B$ lines. Farther along the sequence, G335.78 MM1 displays emission across all three $\Delta E/k_B$. G337.40 (H II) provides an example of a spectrum from more evolved regions, where the emission lines are generally brighter, reflecting a more advanced excitation than in earlier sources. This progression illustrates the increasing complexity of the torsionally excited emission across the evolutionary classification of the clumps.

4. Analysis

4.1. Distribution of ALMA emission and mid-IR counterparts

Figs. 1 – 2 show the ALMA 890 μm dust continuum emission overlaid with the moment-0 contours of the torsionally excited CH_3OH lines for all 12 clumps. The $v_t \geq 1$ emission is generally compact (about one to two synthesized beams) and becomes more extended in more evolved regions (e.g., YSO and H II). In most cases, the $v_t \geq 1$ emission coincides with a single bright

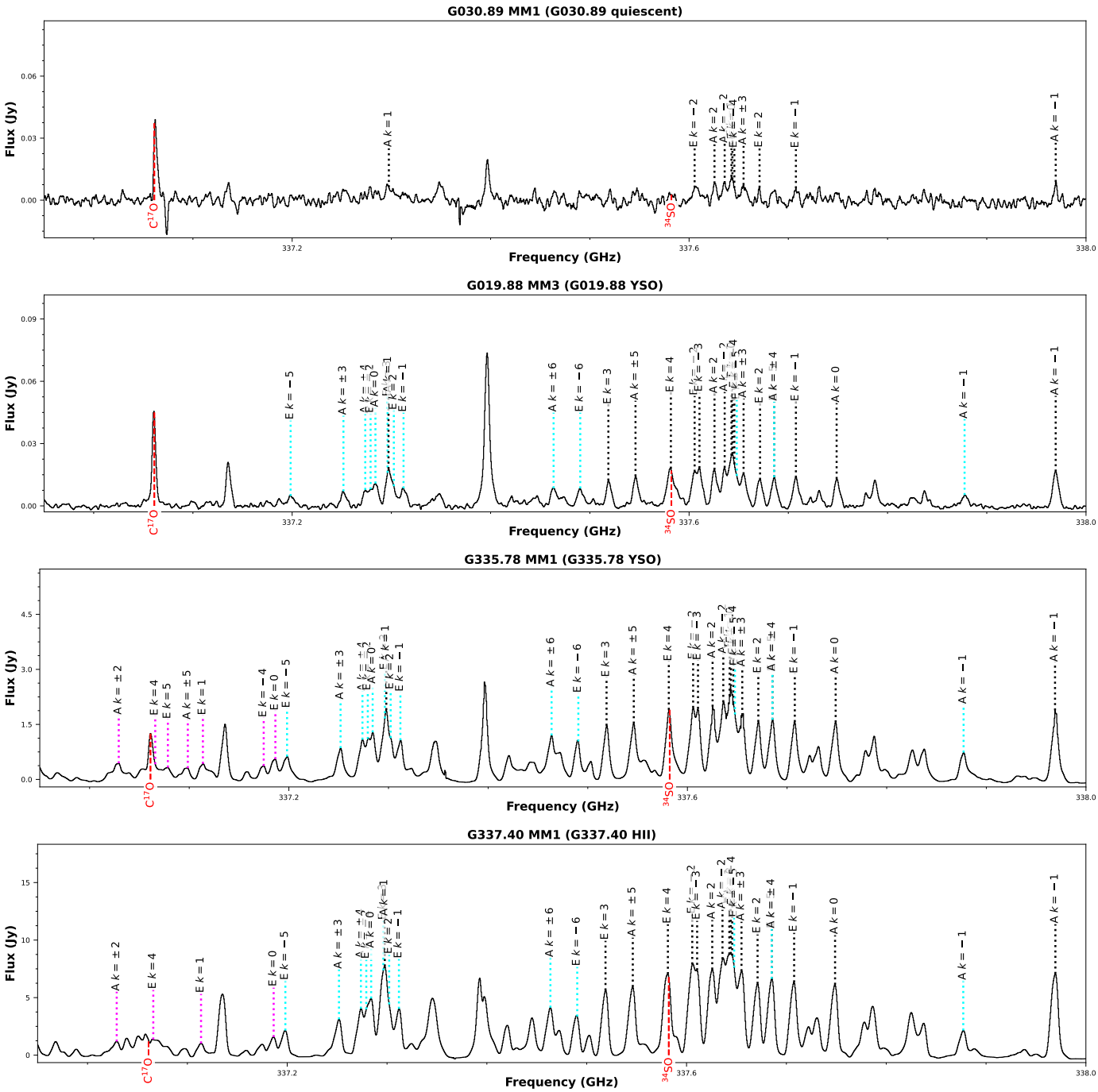

Fig. 3. Four spectra covering 336.950 – 338.000 GHz, showing the CH_3OH $7_k - 6_k$ $v_t \geq 1$ transitions. All clumps are located at similar distances (~3–5 kpc), minimizing distance-related flux variations. The panels illustrate the progressive detection of $v_t \geq 1$ transitions across the sample: G030.89 MM1 ($\sigma \simeq 0.002$ Jy) shows only low-$\Delta E/k_B$ emission; G019.88 MM3 ($\sigma \simeq 0.001$ Jy) displays low- and mid-$\Delta E/k_B$ lines but no significant high-$\Delta E/k_B$ emission; G335.78 MM1 ($\sigma \simeq 0.1$ Jy) and G337.40 MM1 ($\sigma \simeq 0.3$ Jy) exhibit emission in all three $\Delta E/k_B$ ranges, with the latter showing brighter lines. The transitions are labeled with the symmetry species (A or E) and the k quantum number. The low-, mid-, and high-ΔE levels ($E_u/k_B \leq 500$ K, 500 K $< E_u/k_B <$ 750 K, and $E_u/k_B \geq 750$ K, respectively) are shown in black, cyan, and magenta.

890 μm continuum core, although some clumps show multiple cores (e.g., G019.88 and G335.78), as described in Section 3.2.

Since the energy gaps between the torsionally excited levels and the ground state correspond to photons in the ~14–40 μm range, we compared the ALMA line emission with the closest available mid-IR 24 μm images from MIPSGAL. Despite the significant difference in angular resolution between ALMA (≃0.6″) and Spitzer (≃6″), a consistent association is observed between the $v_t \geq 1$ emission (core scale) and the mid-IR emission (clump scale), as shown in Figure C.1.

The only source in the sample without detectable $v_t \geq 1$ emission is G014.49, which also lacks a 24 μm counterpart. All other clumps exhibit $v_t \geq 1$ emission in all three $\Delta E/k_B$, except for the cores G030.89 MM1 and G019.88 MM3, where high-E_u/k_B transitions are not detected.

The spatial association between the line emission and the 24 μm images is clear for six sources: G030.89, G014.19,

Table 3. Detection of CH_3OH $7_k - 6_k$ $v_t \geq 1$ transitions in the observed cores.

Source Name	Core	Position (ICRS) R.A. (J2000) (h : m : s)	Dec. (J2000) (d : m : s)	low-E_u/k_B (356–500) K ~(29–40) μm	mid-E_u/k_B (500–700) K ~ (19–27) μm	high-E_u/k_B ≥700 K ~ (14–19) μm
G030.89	MM1	18:47:13.66	−01:45:03.26	Y	N	N
G014.19	MM1	18:16:58.75	−16:42:14.21	Y	Y	Y
G008.68	MM1	18:06:23.48	−21:37:10.53	Y	Y	Y
G023.21	MM1	18:34:55.20	−08:49:14.86	Y	Y	Y
G335.78	MM1	16:29:47.33	−48:15:52.24	Y	Y	Y
G335.78	MM2	16:29:46.13	−48:15:50.03	Y	Y	Y
G019.88	MM1	18:29:14.36	−11:50:22.52	Y	Y	Y
G019.88	MM2	18:29:14.42	−11:50:24.44	Y	Y	Y
G019.88	MM3	18:29:14.34	−11:50:20.11	Y	Y	N
G337.92	MM1	16:41:10.39	−47:08:03.13	Y	Y	Y
G337.92	MM2	16:41:10.47	−47:08:01.72	Y	Y	Y
G305.21	MM1	13:11:13.72	−62:34:41.27	Y	Y	Y
G301.14	MM1	12:35:35.12	−63:02:31.89	Y	Y	Y
G301.14	MM2	12:35:34.99	−63:02:30.39	Y	Y	Y
G337.40	MM1	16:38:50.47	−47:28:00.46	Y	Y	Y
G343.13	MM1	16:58:17.22	−42:52:07.51	Y	Y	Y
G343.13	MM2	16:58:17.12	−42:52:06.67	Y	Y	N

Notes. The table lists the detection of CH_3OH $7_k - 6_k$ $v_t \geq 1$ transitions in each core, grouped by upper-energy level ($\Delta E/k_B$). The columns for low-, mid-, and high-E_u/k_B levels ($E_u/k_B \leq 500$ K, 500 K $< E_u/k_B <$ 750 K, and $E_u/k_B \geq 750$ K, respectively) indicate whether transitions were detected (Y) or not (N) at $\geq 3\sigma$. Approximate wavelength intervals for each energy range are also provided: low 29–40 μm, mid 19–27 μm, and high 14–19 μm.

G008.68, G023.21, G335.78, and G019.88. The further analysis showed a coincidence with mid-IR compact sources in the MIPSGAL catalog (Gutermuth & Heyer 2015), for which positions and fluxes are provided. We identified two sources with faint 24 μm emission coincident with compact $v_t \geq 1$ emission from two ALMA cores (G030.89 MM1 and G335.78 MM2), for which we estimated the fluxes through aperture photometry. The comparison also revealed multiple compact $v_t \geq 1$ cores, such as in G019.88, which coincide with a single extended emission feature at 24 μm.

In contrast, five clumps (G305.21, G337.92, G301.14, G337.40, and G343.13) are saturated in MIPS images, and the direct comparison between ALMA cores and the 24 μm emission required additional analysis (see Appendix A). These clumps represent the most evolved phases in our sample (one YSO and four H II). To constrain their mid-IR fluxes, we supplemented this analysis with WISE and GLIMPSE images to explore IR emission at complementary wavelengths. More details are provided in Appendix A.

4.2. Correlation between mid-IR and line luminosities

We investigated the line luminosities of $v_t \geq 1$ methanol lines in three $\Delta E/k_B$ regimes in embedded YSOs and examined their relation to the 24 μm mid-IR emission. The methods we used to calculate luminosities are described in Appendix A.2.

To account for differences in initial chemical conditions of each source, we normalized the line luminosities by the methanol abundance, X_{CH_3OH}, adopting values reported by Giannetti et al. (2017) that range from 0.4×10^{-8} to 10.6×10^{-8}, indicating that methanol is abundant even in cold environments. For G305.21, where no specific abundance estimate is available, we adopted a median value of 2.3×10^{-8}, representative of intermediate-stage (IRb or YSO) clumps from the same study. Although it is not source-specific, this median value provides a reasonable first-order approximation and ensures a homogeneous scaling across the sample.

Due to their different angular resolutions, ALMA and mid-IR observations probe distinct spatial scales, from cores to clumps. In some regions, a single ALMA core corresponds to one MIPSGAL source (e.g., G014.19 or G008.68), while in others, multiple ALMA cores are associated with a single extended mid-IR source (e.g., G019.88). For saturated MIPS images, we derived conservative lower limits to the mid-IR luminosities (except for G343.13), with complementary WISE measurements providing upper limits (except for G337.92 and G343.13). To ensure a consistent comparison, we summarize the line luminosities of all ALMA cores associated with each mid-IR source (see Table B.2).

To explore the relation between $v_t \geq 1$ and 24 μm luminosities, we performed a power-law fit in log-log space,

$$\log_{10}\left(\frac{L(\Delta E/k_B)}{X_{CH_3OH}}\right) = \alpha + \beta \log_{10}(L_{MIR}), \quad (1)$$

where α is the intercept, and β is the slope, $L(\Delta E/k_B)/X_{CH_3OH}$ represents the normalized $v_t \geq 1$ methanol line luminosity in the three $\Delta E/k_B$ regimes, and L_{MIR} is the 24 μm luminosity (Appendix A.2).

We performed a Bayesian linear regression using the package PyMC[10] (Salvatier et al. 2016; Patil et al. 2010), which includes propagated measurement uncertainties and an intrinsic scatter term. Normal priors on the intercept and slope were centered on the initial linear fit estimates. Censored data (lower and upper limits) were incorporated into the model using conservative lower limits from MIPS and upper limits from WISE. We included them to account for sources with saturated mid-IR fluxes. We also performed a model comparison to assess whether a constant (slope = 0) or a linear (nonzero slope) model described the

[10] https://www.pymc.io/

data better. The resulting odds ratio of ∼10 for low-energy transitions indicates moderate evidence in favor of the linear relation.

The log$L$ – log$L$ diagrams with the resulting fits are shown in Fig. 4 and the best-fit slopes and intercepts with their credible intervals (CI) are summarized in Table 4. In all three $\Delta E/k_B$ regimes corresponding to mid-IR wavelengths of low 29–40 μm, mid 19–27 μm, and high 14–19 μm, the slopes are consistent within the uncertainties, ranging from ∼0.4 to 0.6, suggesting that the $v_t \geq 1$ methanol lines likely trace a common excitation mechanism despite differences in excitation energy. Since these transitions are radiatively excited by mid-IR photons, the trend might also reflect the mid-IR radiation field of the sources.

For visualization purposes, Fig. 4 also indicates expected 24 μm luminosities for saturated sources derived from GLIMPSE fluxes (see Appendix A.1).

5. Discussion

Our pilot sample was chosen to test the hypothesis that CH_3OH $v_t \geq 1$ lines are radiatively excited by mid-IR photons and can serve as indirect tracers of the mid-IR radiation fields around YSOs in different evolutionary stages. Based on the source classification, we expected that mid-IR quiescent sources would not show $v_t \geq 1$ lines because either the absence of protostellar activity or its very early stages leaves the dust too cold to emit significant mid-IR radiation. Conversely, more evolved sources are expected with stronger mid-IR fields capable of efficiently populating the torsional levels. Consistent with these expectations, the only clump (G014.49) without $v_t \geq 1$ lines also lacks 24 μm emission. In contrast, G030.89, previously classified as quiescent, exhibits faint 24 μm emission along with detectable $v_t \geq 1$ lines (Appendix A.1). Based on these observations, we reclassified it as protostellar, further supporting the interpretation that these lines are sensitive tracers of embedded protostellar activity.

The power-law correlation between $L(\Delta E/k_B)/X_{CH_3OH}$ and mid-IR luminosity across different $\Delta E/k_B$ is promising (Fig. 4). This relation appears largely independent of distance because all sources are within a relatively narrow range of ∼3–5 kpc. Variations in the initial conditions are mitigated because the normalization by X_{CH_3OH} accounts for abundance differences. However, several factors can limit the conclusions that can be drawn from the observed trend. The sample is statistically small, the lowest-luminosity objects are underrepresented, and they also tend to exhibit weak or undetected high-E_u/k_B lines. This likely affects the slope steepness. In contrast, the brightest more evolved sources are saturated in the mid-IR, which only provides lower and upper limits on the slope. Consequently, a larger sample, particularly of low-luminosity sources, is needed to refine the slope and further assess the dependences of the relation. Giannetti et al. (2017) found that gas temperatures derived from CH_3OH $v_t \geq 1$ transitions correlate more closely with 22 μm luminosities than with bolometric luminosities, suggesting a local excitation mechanism linked to internal protostellar heating at the clump scale. Our log$L$ – log$L$ diagrams similarly show a linear trend between the luminosities of $v_t \geq 1$ lines and 24 μm emission, confirming the sensitivity of these lines to the local mid-IR environment. We verified that the trend persists across 22–70 μm luminosities from available catalogs, whereas no correlation is observed with 8 μm, consistent with the idea that these lines indirectly trace mid-IR photons with longer wavelengths, which excite them in the local radiation field of MYSOs. As a result, the power-law trend suggests that these lines might also serve as quantitative proxies for internal mid-IR radiation fields, and by extension, for the evolutionary stages of the sources. A

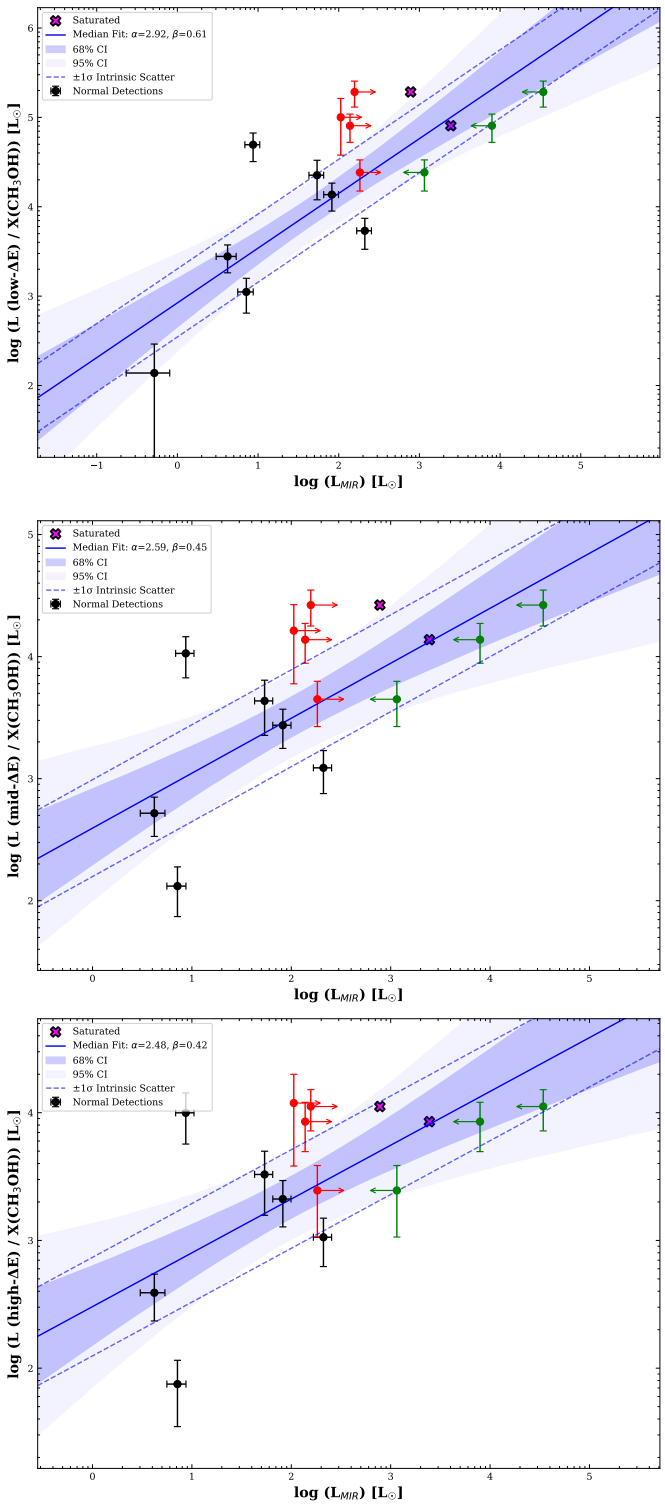

Fig. 4. log$L$ – log$L$ diagrams showing the relation between the mid-IR luminosity (L_{MIR}) and the methanol $v_t \geq 1$ line luminosity normalized by the methanol abundance of the clump, $L(\Delta E/k_B)/X_{CH_3OH}$, in the low (upper panel), mid (middle panel), and high (bottom panel) $\Delta E/k_B$ regimes. The best-fit power-law relation (blue line) was obtained using Bayesian linear regression in log-log space. The dark and light shaded blue regions represent the 68% and 95% credible intervals (CI) of the regression, derived from the posterior distribution of the slope and intercept, accounting for their uncertainties. The symbols represent sources with observed luminosities (black). For saturated sources, we show lower limits from MIPSGAL at 24 μm (red), upper limits from WISE at 22 μm (green), and, for visualization purposes only, expected fluxes scaled from JWST template ratios (magenta crosses; see Appendix A.1).

Table 4. Results of the Bayesian linear regression.

$\Delta E/k_B$	α	68% CI (α)	95% CI (α)	β	68% CI (β)	95% CI (β)
low	2.92	2.65 – 3.20	2.38 – 3.47	0.61	0.49 – 0.74	0.38 – 0.89
mid	2.59	2.29 – 2.92	2.00 – 3.26	0.45	0.32 – 0.58	0.18 – 0.72
high	2.48	2.18 – 2.80	1.85 – 3.13	0.42	0.29 – 0.56	0.16 – 0.71

Notes. Best-fit parameters (median coefficient α intercept, β slope) and their 68% and 95% credible intervals (CI) for the Bayesian power-law fit in log-log space between $L(\Delta E/k_B)/X_{CH_3OH}$ and L_{MIR} at different $\Delta E/k_B$.

similar approach was adopted by Aalto et al. (2015), who used vibrationally excited HCN lines to infer mid-IR luminosities in extragalactic sources.

Our results are consistent with the radiative transfer modeling by Leurini et al. (2007b), who suggested that these transitions are almost exclusively driven by radiative pumping, while collisional excitation remains inefficient even at very high densities (10^{10}–10^{11} cm^{-3}). The co-location of $v_t \geq 1$ emission with the 24 μm sources and the 890 μm ALMA continuum brightest peaks implies that excitation occurs in dense compact regions in the immediate vicinity of the protostar. This finding reinforces the interpretation that CH_3OH $v_t \geq 1$ transitions probe the innermost environment of protostars, where radiative feedback dominates collisional processes. The $v_t \geq 1$ lines are indeed pumped by photons at energies similar to those in Class II methanol masers (Menten et al. 1986), which trace the inner gas close to massive YSOs and are found in outer regions of disk winds (e.g., Sanna et al. 2015). Similarly, Leurini et al. (2016) observed CH_3OH v_t=2 lines in the low-mass protostar HH 212. In this source, the emission traces velocity gradients consistent with rotating and expanding gas, which was interpreted as a disk wind by the authors. In the high-mass protocluster IRAS 05358+3543, Leurini et al. (2007a) observed double-peaked $v_t \geq 1$ profiles, which are indicative of disks. These studies suggested that CH_3OH $v_t \geq 1$ transitions trace the innermost rotating structures at the base of outflows, likely launched near the disk surface, across a broad range of stellar masses. A simultaneous study of torsionally excited methanol lines and Class II masers at a comparable resolution might confirm the origin of the two emissions from the same gas and further support the idea that they are both pumped by the same mechanism.

The low angular resolution of Spitzer/MIPS limits our ability to distinguish whether the 24 μm emission arises from a single dominant core or from multiple embedded cores. Consequently, in the log$L$ – log$L$ diagram, we compare the total $v_t \geq 1$ line luminosities from individual cores with a 24 μm luminosity representing the entire clump. This introduces uncertainties in interpretation. This pilot study highlights the potential of torsionally excited methanol lines as tracers of internal radiative feedback, but further ALMA and high-resolution mid-IR observations (e.g., with JWST) are needed to support this hypothesis. It is essential to extend the analysis to a larger statistically significant sample, particularly including low-luminosity sources to refine the slope of the log$L$ – log$L$ diagram and to better understand the earliest stages of high-mass star formation.

6. Summary and conclusions

We investigated the excitation and spatial distribution of CH_3OH $v_t \geq 1$ lines in a sample of high-mass star-forming regions by comparing ALMA spectral line and continuum observations at 890 μm with mid-IR data.

Our results show that CH_3OH $v_t \geq 1$ emission is compact and systematically associated with ALMA continuum peaks and 24 μm sources, indicating a close spatial association with embedded protostellar objects. The only clump without mid-IR counterparts shows no torsionally excited methanol emission, consistent with radiative pumping as the dominant excitation mechanism. In a few cases, weak 24 μm emission coincides with weak $v_t \geq 1$ lines, suggesting that these transitions can reveal faint embedded protostars that are difficult to identify in mid-IR images due to confusion and limited angular resolution.

The correlation between methanol lines and 24 μm luminosities, which persists across multiple excitation ranges and is largely independent of the methanol abundance variations, reinforces the interpretation that local mid-IR radiation from warm dust dominates the excitation of these transitions. This supports the hypothesis that methanol $v_t \geq 1$ lines are reliable probes of the internal radiation environment of YSOs at the core scale and, by extension, their evolutionary stage.

In summary, CH_3OH $v_t \geq 1$ transitions provide an effective tool for identifying and characterizing embedded star formation and probing internal radiative feedback. Future high-resolution mid-IR observations, for instance, with JWST, combined with statistically significant surveys, will be essential to refine this diagnostic, extend its application to diverse environments and mass regimes, and improve our understanding of the earliest stages of protostellar evolution.

Acknowledgements. We dedicate this work to Karl M. Menten, whose profound expertise in this field laid the foundations of this study: his commitment, insight, and unwavering enthusiasm continue to inspire us and guide our research. We thank Prof. G. Malloci for his constructive comments and support during the development of this study. We are grateful to R. Paladino for the useful support and discussion. We thank the Italian ARC node and the staff for the support in data reduction. We thank the anonymous referee for constructive comments that improved the clarity of this paper. This work has been supported by the project PRIN-INAF 2016 "From yOuNg Star clusters to planETary systems (ONSET)". This publication has received funding from the European Union's Horizon 2020 research and innovation program under grant agreement No 101004719 (ORP). C.S. acknowledges the support from the European Southern Observatory (ESO) Early-Career Scientific Visitor Programme Garching (Germany). This paper makes use of the following ALMA data: ADS/JAO.ALMA#2017.1.00377.S. ALMA is a partnership of ESO (representing its member states), NSF (USA) and NINS (Japan), together with NRC (Canada), MOST and ASIAA (Taiwan) and KASI (Republic of Korea), in co-operation with the Republic of Chile. The Joint ALMA Observatory is operated by ESO, AUI/NRAO and NAOJ. This work used `Astropy`[11], a community developed core Python package for Astronomy (Astropy Collaboration 2013, 2018, 2022); `APLPY` (Robitaille & Bressert 2012; Robitaille 2019); `matplotlib` (Hunter 2007); `NumPy` (Harris et al. 2020), `SciPy` (Virtanen et al. 2020), and CARTA software (Comrie et al. 2021; Ott et al. 2022) This research used the VizieR catalog, operated at CDS, Strasbourg, France. This document was prepared using the Overleaf web platform[12].

References

Aalto, S., Martín, S., Costagliola, F., et al. 2015, A&A, 584, A42

[11] `http://www.astropy.org`

[12] Overleaf is available at `https://www.overleaf.com`.

Alexov, A., Berriman, G. B., Chiu, N.-M., et al. 2005, in Astronomical Society of the Pacific Conference Series, Vol. 347, Astronomical Data Analysis Software and Systems XIV, ed. Shopbell, P., Britton, M., & Ebert, R., 7
André, P., Minier, V., Gallais, P., et al. 2008, A&A, 490, L27
André, P., Ward-Thompson, D., & Barsony, M. 1993, ApJ, 406, 122
André, P., Ward-Thompson, D., & Barsony, M. 2000, in Protostars and Planets IV, ed. Mannings, V., Boss, A. P., & Russell, S. S., 59
Astropy Collaboration. 2013, A&A, 558, A33
Astropy Collaboration. 2018, AJ, 156, 123
Astropy Collaboration. 2022, AJ, 163, 286
Beltrán, M. T., Sánchez-Monge, Á., Cesaroni, R., et al. 2014, A&A, 571, A52
Benjamin, R. A., Churchwell, E., Babler, B. L., et al. 2003, PASP, 115, 953
Beuther, H., Kuiper, R., & Tafalla, M. 2025, ARA&A, 63, 1
Beuther, H., van Dishoeck, E. F., Tychoniec, L., et al. 2023, A&A, 673, A121
Billington, S. J., Urquhart, J. S., König, C., et al. 2019, MNRAS, 490, 2779
Bontemps, S., André, P., Terebey, S., & Cabrit, S. 1996, in Disks and Outflows Around Young Stars, ed. Beckwith, S., Staude, J., Quetz, A., & Natta, A., Vol. 465 (Springer-Verlag Berlin Heidelberg New York), 270
Braatz, J. 2020, ALMA Cycle 8 Proposer's Guide, ALMA Observatory
Bradley, L., Sipőcz, B., Robitaille, T., et al. 2022, astropy/photutils: 1.6.0
Carey, S. J., Noriega-Crespo, A., Mizuno, D. R., et al. 2009, PASP, 121, 76
Carey, S. J. et al. 2007, MIPSGAL v2.0 Data Delivery Description Document (16 October 2007), accessed: 2025-11-28
Carroll, T. J. & Goldsmith, P. F. 1981, ApJ, 245, 891
CASA Team, Bean, B., Bhatnagar, S., et al. 2022, PASP, 134, 114501
Chen, L., Qin, S.-L., Liu, T., et al. 2025, A&A, 694, A166
Churchwell, E., Babler, B. L., Meade, M. R., et al. 2009, PASP, 121, 213
Coletta, A., Molinari, S., Schisano, E., et al. 2025, A&A, 696, A151
Comrie, A., Wang, K.-S., Hsu, S.-C., et al. 2021, CARTA: The Cube Analysis and Rendering Tool for Astronomy
Contreras, Y., Schuller, F., Urquhart, J. S., et al. 2013, A&A, 549, A45
Csengeri, T., Leurini, S., Wyrowski, F., et al. 2016, A&A, 586, A149
Csengeri, T., Urquhart, J. S., Schuller, F., et al. 2014, A&A, 565, A75
Cutri, R. M., Wright, E. L., Conrow, T., et al. 2012, Explanatory Supplement to the WISE All-Sky Data Release Products, Explanatory Supplement to the WISE All-Sky Data Release Products
Elia, D., Molinari, S., Schisano, E., et al. 2017, MNRAS, 471, 100
Elia, D., Schisano, E., Molinari, S., et al. 2010, A&A, 518, L97
Evans, II, N. J., Dunham, M. M., Jørgensen, J. K., et al. 2009, ApJS, 181, 321
Francis, L., Johnstone, D., Herczeg, G., Hunter, T. R., & Harsono, D. 2020, AJ, 160, 270
Giannetti, A., Leurini, S., Wyrowski, F., et al. 2017, A&A, 603, A33
Giannetti, A., Wyrowski, F., Brand, J., et al. 2014, A&A, 570, A65
Goldsmith, P. F., Krotkov, R., Snell, R. L., Brown, R. D., & Godfrey, P. 1983, ApJ, 274, 184
Goldsmith, P. F., Snell, R. L., Deguchi, S., Krotkov, R., & Linke, R. A. 1982, ApJ, 260, 147
Güsten, R., Nyman, L. Å., Schilke, P., et al. 2006, A&A, 454, L13
Gutermuth, R. A. & Heyer, M. 2015, AJ, 149, 64
Harris, C. R., Millman, K. J., van der Walt, S. J., et al. 2020, Nature, 585, 357
Hatchfield, H. P., Battersby, C., Keto, E., et al. 2020, ApJS, 251, 14
Hoare, M. G., Purcell, C. R., Churchwell, E. B., et al. 2012, PASP, 124, 939
Hunter, J. D. 2007, Computing in Science and Engineering, 9, 90
Hunter, T. R., Indebetouw, R., Brogan, C. L., et al. 2023, PASP, 135, 074501
Kennicutt, R. C. & Evans, N. J. 2012, ARA&A, 50, 531
König, C., Urquhart, J. S., Csengeri, T., et al. 2017, A&A, 599, A139
Krumholz, M. R. 2014, Phys. Rep., 539, 49
Lada, C. J., Margulis, M., & Dearborn, D. 1984, ApJ, 285, 141
Leurini, S., Beuther, H., Schilke, P., et al. 2007a, A&A, 475, 925
Leurini, S., Codella, C., Cabrit, S., et al. 2016, A&A, 595, L4
Leurini, S., Schilke, P., Wyrowski, F., & Menten, K. M. 2007b, A&A, 466, 215
Ma, B., Tan, J. C., & Barnes, P. J. 2013, ApJ, 779, 79
McElwain, M. W., Feinberg, L. D., Perrin, M. D., et al. 2023, PASP, 135, 058001
McKee, C. F. & Ostriker, E. C. 2007, ARA&A, 45, 565
McMullin, J. P., Waters, B., Schiebel, D., Young, W., & Golap, K. 2007, in Astronomical Society of the Pacific Conference Series, Vol. 376, Astronomical Data Analysis Software and Systems XVI, ed. Shaw, R. A., Hill, F., & Bell, D. J., 127
Menten, K. M., Walmsley, C. M., Henkel, C., et al. 1986, A&A, 169, 271
Molinari, S., Merello, M., Elia, D., et al. 2016, ApJ, 826, L8
Molinari, S., Pezzuto, S., Cesaroni, R., et al. 2008, A&A, 481, 345
Molinari, S., Schilke, P., Battersby, C., et al. 2025, A&A, 696, A149
Molinari, S., Swinyard, B., Bally, J., et al. 2010, A&A, 518, L100
Motte, F., Bontemps, S., Csengeri, T., et al. 2022, A&A, 662, A8
Motte, F., Bontemps, S., & Louvet, F. 2018, ARA&A, 56, 41
Motte, F., Bontemps, S., Schilke, P., et al. 2007, A&A, 476, 1243
Müller, H. S. P., Schlöder, F., Stutzki, J., et al. 2005, in IAU Symposium, Vol. 231, Astrochemistry: Recent Successes and Current Challenges, ed. Lis, D. C., Blake, G. A., & Herbst, E., 62
Müller, H. S. P., Thorwirth, S., Roth, D. A., & Winnewisser, G. 2001, A&A, 370, L49
Nayak, O., Hirschauer, A. S., Kavanagh, P. J., et al. 2024, ApJ, 963, 94
Ott, J., Raba, R., & Hibbard, J. 2022, in American Astronomical Society Meeting Abstracts, Vol. 240, American Astronomical Society Meeting #240, 215.05
Patil, A., Huard, D., & Fonnesbeck, C. J. 2010, Journal of Statistical Software, 35, 1
Pickett, H. M., Poynter, R. L., Cohen, E. A., et al. 1998, J. Quant. Spectr. Rad. Transf., 60, 883
Pilbratt, G. L., Riedinger, J. R., Passvogel, T., et al. 2010, A&A, 518, L1
Price, S. D., Egan, M. P., Carey, S. J., Mizuno, D. R., & Kuchar, T. A. 2001, AJ, 121, 2819
Purcell, C. R., Hoare, M. G., Cotton, W. D., et al. 2013, ApJS, 205, 1
Remijan, A., Biggs, A., Cortes, P. A., et al. 2019, ALMA Technical Handbook,ALMA Doc. 7.3, ver. 1.1, 2019, ALMA Technical Handbook,ALMA Doc. 7.3, ver. 1.1ISBN 978-3-923524-66-2
Remijan, A. J., Markwick-Kemper, A., & ALMA Working Group on Spectral Line Frequencies. 2007, in American Astronomical Society Meeting Abstracts, Vol. 211, American Astronomical Society Meeting Abstracts, 132.11
Rigby, A. J., Peretto, N., Anderson, M., et al. 2024, MNRAS, 528, 1172
Robitaille, T. 2019, APLpy v2.0: The Astronomical Plotting Library in Python
Robitaille, T. & Bressert, E. 2012, APLpy: Astronomical Plotting Library in Python, Astrophysics Source Code Library, record ascl:1208.017
Robitaille, T., Rice, T., Beaumont, C., et al. 2019, astrodendro: Astronomical data dendrogram creator, Astrophysics Source Code Library, record ascl:1907.016
Robitaille, T. P., Whitney, B. A., Indebetouw, R., Wood, K., & Denzmore, P. 2006, ApJS, 167, 256
Rosolowsky, E. W., Pineda, J. E., Kauffmann, J., & Goodman, A. A. 2008, ApJ, 679, 1338
Russeil, D., Zavagno, A., Motte, F., et al. 2010, A&A, 515, A55
Salvatier, J., Wiecki, T. V., & Fonnesbeck, C. 2016, PyMC3: Python probabilistic programming framework, Astrophysics Source Code Library, record ascl:1610.016
Sánchez-Monge, Á., Beltrán, M. T., Cesaroni, R., et al. 2014, A&A, 569, A11
Sanna, A., Surcis, G., Moscadelli, L., et al. 2015, A&A, 583, L3
Saraceno, P., André, P., Ceccarelli, C., Griffin, M., & Molinari, S. 1996, A&A, 309, 827
Schuller, F., Menten, K. M., Contreras, Y., et al. 2009, A&A, 504, 415
Sobolev, A. M. & Deguchi, S. 1994, A&A, 291, 569
Spitzer Science, C. 2009, VizieR Online Data Catalog: GLIMPSE Source Catalog (I + II + 3D) (IPAC 2008), VizieR On-line Data Catalog: II/293. Originally published in: IPAC, Caltech (2008)
Tan, J. C., Beltrán, M. T., Caselli, P., et al. 2014, in Protostars and Planets VI, ed. Beuther, H., Klessen, R. S., Dullemond, C. P., & Henning, T., 149–172
Teplitz, H. I., Howell, J., Desai, V., & IRSA Team. 2018, in The Cosmic Wheel and the Legacy of the AKARI Archive: From Galaxies and Stars to Planets and Life, ed. Ootsubo, T., Yamamura, I., Murata, K., & Onaka, T., 25–28
Urquhart, J. S., Busfield, A. L., Hoare, M. G., et al. 2007, A&A, 461, 11
Urquhart, J. S., Csengeri, T., Wyrowski, F., et al. 2014, A&A, 568, A41
Urquhart, J. S., Hoare, M. G., Purcell, C. R., et al. 2009, A&A, 501, 539
Urquhart, J. S., König, C., Giannetti, A., et al. 2018, MNRAS, 473, 1059
Urquhart, J. S., Thompson, M. A., Moore, T. J. T., et al. 2013, MNRAS, 435, 400
Urquhart, J. S., Wells, M. R. A., Pillai, T., et al. 2022, MNRAS, 510, 3389
Virtanen, P., Gommers, R., Burovski, E., et al. 2020, scipy/scipy: SciPy 1.6.0
Wallace, J., Kolz, T., Battersby, C., et al. 2026, ApJ, 998, 302
Walsh, A. J., Burton, M. G., Hyland, A. R., & Robinson, G. 1999, MNRAS, 309, 905
Wienen, M., Wyrowski, F., Menten, K. M., et al. 2015, A&A, 579, A91
Wienen, M., Wyrowski, F., Walmsley, C. M., et al. 2021, A&A, 649, A21
Wright, E. L., Eisenhardt, P. R. M., Mainzer, A. K., et al. 2010, AJ, 140, 1868
Wyrowski, F., Schilke, P., & Walmsley, C. M. 1999, A&A, 341, 882
Zinnecker, H. & Yorke, H. W. 2007, ARA&A, 45, 481

Appendix A: Methods

A.1. Infrared images analysis

To analyze the distribution of the mid-IR emission, we first visually compared ALMA emission with MIPS 24 μm images using the Cube Analysis and Rendering Tool for Astronomy software (CARTA; Comrie et al. 2021; Ott et al. 2022). Among the sources, G014.49 is the only one without detectable 24 μm emission. We divided the sources into two categories: those with detectable 24 μm emission (G030.89, G014.19, G008.68, G023.21, G335.78, G019.88), and those with saturated emission (G337.92, G305.21, G301.14, G337.40, G343.13).

We used the Vizier catalog (Gutermuth & Heyer 2015) to extract MIPSGAL sources within a radius of ~6″ from the ATLASGAL clump positions, obtaining their positions and fluxes. Sources G014.19, G008.68, G023.21, and G335.78 were already cataloged. While for two new 24 μm detections (G030.89 MM1 and G335.78 MM2), we performed aperture photometry using the photutils Python package (Bradley et al. 2022), adopting the parameters[13] recommended by Gutermuth & Heyer (2015).

In detail, G030.89 MM1, previously classified as quiescent by Urquhart et al. (2022), shows faint 24 μm emission (~0.06 Jy), close to the 5σ detection threshold of 1.7 Jy (Carey et al. 2007), which likely explains why it was not detected in previous searches. Associated with G335.78, a second compact mid-IR source G335.78 MM2 (~0.1 Jy), is detected 12″ from the brighter G335.78 MM1 (the cataloged MIPSGAL source). We classified G030.89 MM1 and G335.78 MM2 as protostellar according to the criteria of Urquhart et al. (2022).

Although the angular resolutions of ALMA and MIPSGAL are different, the ALMA emission generally matches the cataloged MIPSGAL centroids within the MIPS beam size (~6″). However, in the case of G019.88, a slight shift is observed between the ALMA cores peaks and the MIPSGAL centroid. This source shows an asymmetric elliptical distribution at 24 μm, with the emission peak aligning with the ALMA data, while the MIPSGAL centroid is offset, likely due to the 2D Gaussian method for source identification and systematic astrometric corrections (Gutermuth & Heyer 2015).

For sources with severe saturation, where MIPSGAL images saturate at ~1700 MJy sr^{-1} (Carey et al. 2009) (typically in bright YSOs or H II regions), we examined MIPS images and supplemented with WISE and GLIMPSE images. We estimated conservative lower limits for their fluxes by replacing the saturated (NaN) pixels in MIPS images with the maximum intensity from nearby non-saturated regions and performing aperture photometry on the corrected maps, using the same parameters described for unsaturated sources. We applied this method to G305.21, G301.14, G337.40, and G343.13, where saturation affected only a limited region. However, it was not applicable to G337.92, where most of the image was saturated.

We also examined the WISE images and catalog data (Cutri et al. 2012) within a radius of ~6″ from the ATLASGAL clump positions, and identified three sources: G301.14, G337.40, and G343.13. For the remaining saturated sources (G337.92 and G305.21), we could not determine fluxes due to diffuse and extended emission, and no aperture photometry was performed. Similarly, we inspected IRAC images and the GLIMPSE catalog (Spitzer Science 2009) within a radius of ~2″ from the ATLASGAL clump positions, identifying two sources: G301.14 and G337.40. Fluxes at 8 μm were available only for G337.40 in the catalog. For G301.14, we performed aperture photometry following the IRAC Instrument Handbook[14]. A summary table of all IR fluxes used in this work is provided in Table B.2.

For saturated sources with available 22 μm and 8 μm fluxes, we estimated the 24 μm fluxes using scaling factors derived from JWST spectroscopic observations of massive protoclusters in our Galaxy (Beuther et al. 2023) and in the Large Magellanic Cloud (Nayak et al. 2024), spanning the spectral range of ~5–28 μm. Specifically, the ratio of 24 μm/22 μm fluxes ranges from ~0.9 to 1.4, with a mean value of 1.24. The ratio of 24 μm/8 μm fluxes ranges from ~28 to ~220, with a mean value of 100. In Fig. 4, flux estimates derived from WISE are used as upper limits, while those from GLIMPSE are used only for visualization purposes.

A.2. Lines and IR luminosities

This section describes the methodology adopted to compute the luminosities of the $v_t \geq 1$ methanol lines (list of transitions in Table B.1) and the mid-IR continuum emission at 24 μm.

The total luminosity of each source for a given $\Delta E/k_B$ is computed by summing the contributions from each 890 μm continuum core, integrating over all $v_t \geq 1$ methanol lines within that specific $\Delta E/k_B$ range.

$$L(\Delta E/k_B) = 4\pi d^2 \sum_i \left(\int_{\Delta\nu_i} I_{v_t \geq 1}\, d\nu \right) \quad [erg\ s^{-1}], \tag{A.1}$$

where d is the distance to the source (in kpc), $\Delta\nu_i$ is the linewidth for the i-th methanol line (in MHz), $I_{v_t \geq 1}$ is the intensity of the methanol line at a frequency ν (in Jy), the sum is taken over all ALMA cores indexed by i.

For the mid-IR continuum luminosity at 24 μm, we used the following formula:

$$L_{\rm MIR} = 4\pi d^2\, \nu f_\nu \quad [erg\ s^{-1}], \tag{A.2}$$

where ν is the central frequency of the MIPS 24 μm band (in Hz) and f_ν is the flux density at 24 μm (in Jy) from the MIPSGAL catalog or derived from WISE or GLIMPSE (see details in Appendix A.1).

For comparison, we converted the calculated luminosities into solar units ($L_\odot$).

[13] Aperture radius: 6.35″; background annulus: 7.62″–17.78″; aperture correction factor: 1.63.

[14] Aperture radius: 2.4″; background annulus: 2.4″–7.2″; aperture correction factor: 1.568.

Appendix B: Supplementary tables

Table B.1. List of torsionally excited CH_3OH transitions analyzed in this paper.

Rest Frequency (MHz)	CH_3OH transition	E_u/k_B (K)
337463.703	$7_6 - 6_6$ A^+ $v_t = 1$	533.0
337463.703	$7_6 - 6_6$ A^- $v_t = 1$	533.0
337490.562	$7_{-6} - 6_{-6}$ E $v_t = 1$	558.2
337519.138	$7_3 - 6_3$ E $v_t = 1$	482.2
337546.116	$7_5 - 6_5$ A^+ $v_t = 1$	485.3
337546.116	$7_5 - 6_5$ A^- $v_t = 1$	485.3
337605.288	$7_{-2} - 6_{-2}$ E $v_t = 1$	429.4
337610.661	$7_{-3} - 6_{-3}$ E $v_t = 1$	387.4
337610.68	$7_6 - 6_6$ E $v_t = 1$	657.1
337625.753	$7_2 - 6_2$ A^+ $v_t = 1$	363.4
337635.754	$7_2 - 6_2$ A^- $v_t = 1$	363.4
337642.478	$7_1 - 6_1$ E $v_t = 1$	356.2
337643.915	$7_0 - 6_0$ E $v_t = 1$	365.4
337646.042	$7_{-4} - 6_{-4}$ E $v_t = 1$	470.2
337648.209	$7_{-5} - 6_{-5}$ E $v_t = 1$	610.9
337655.199	$7_3 - 6_3$ A^+ $v_t = 1$	460.9
337655.236	$7_3 - 6_3$ A^- $v_t = 1$	460.9
337671.238	$7_2 - 6_2$ E $v_t = 1$	464.7
337685.248	$7_5 - 6_5$ E $v_t = 1$	493.9
337685.614	$7_4 - 6_4$ A^{+-} $v_t = 1$	545.8
337707.568	$7_{-1} - 6_{-1}$ E $v_t = 1$	478.2
337748.83	$7_0 - 6_0$ A $v_t = 1$	488.4
337969.438	$7_{-1} - 6_{-1}$ A^- $v_t = 1$	390.1
336605.889	$7_1 - 6_1$ A^+ $v_t = 2$	747.4
336970.183	$7_6 - 6_6$ A^{+-} $v_t = 2$	1022.6
337021.917	$7_{-3} - 6_{-3}$ E $v_t = 2$	979.7
337029.573	$7_2 - 6_2$ E $v_t = 2$	941.3
337029.662	$7_{-2} - 6_{-2}$ E $v_t = 2$	941.3
337098.918	$7_5 - 6_5$ A^+- $v_t = 2$	935.1
337113.868	$7_1 - 6_1$ E $v_t = 2$	863.6
337159.158	$7_6 - 6_6$ E $v_t = 2$	762.8
337175.097	$7_{-4} - 6_{-4}$ E $v_t = 2$	809.2
337186.488	$7_0 - 6_0$ E $v_t = 2$	798.9
337252.172	$7_3 - 6_3$ A^- $v_t = 2$	722.8
337252.173	$7_3 - 6_3$ A^+ $v_t = 2$	722.8
337273.561	$7_4 - 6_4$ A^+ $v_t = 2$	679.2
337279.18	$7_{-2} - 6_{-2}$ E $v_t = 2$	709.6
337284.32	$7_0 - 6_0$ A^+ $v_t = 2$	572.9
337312.36	$7_{-1} - 6_{-1}$ E $v_t = 2$	596.7

Table B.2. Infrared fluxes of the selected sources.

Name	Core	Flux 24 μm (Jy)	Flux 22 μm (Jy)	Flux 8 μm (Jy)
G030.89	MM1	0.006[b]		
G014.19	MM1	0.188[c]	0.174[c]	
G008.68	MM1	0.703[c]	0.5783[c]	
G023.21	MM1	0.104[c]		
G335.78	MM1	1.91[c]	1.4[c]	
G335.78	MM2	0.097[b]		
G019.88	MM1 + MM2 + MM3	4.884[c]	5.35[c]	0.720[c]
G337.92[a]	MM1 + MM2			
G305.21[a]	MM1	>2.134[d]		
G301.14[a]	MM1 + MM2	>2.699[d]	301[c]	0.107[b]
G337.40[a]	MM1	>4.932[d]	143[c]	0.692[c]
G343.13[a]	MM1 + MM2	>8.028[d]	25.7[c]	

Notes. The indices indicate: [(a)] saturated sources in MIPSGAL images; [(b)] fluxes measured in this work via aperture photometry; [(c)] fluxes taken directly from the MIPSGAL (24 μm, Gutermuth & Heyer 2015), WISE (22 μm, Cutri et al. 2012) and GLIMPSE (8 μm, Spitzer Science 2009) catalogs; [(d)] conservative lower limits for saturated sources in the 24 μm maps.

Appendix C: Supplementary figures

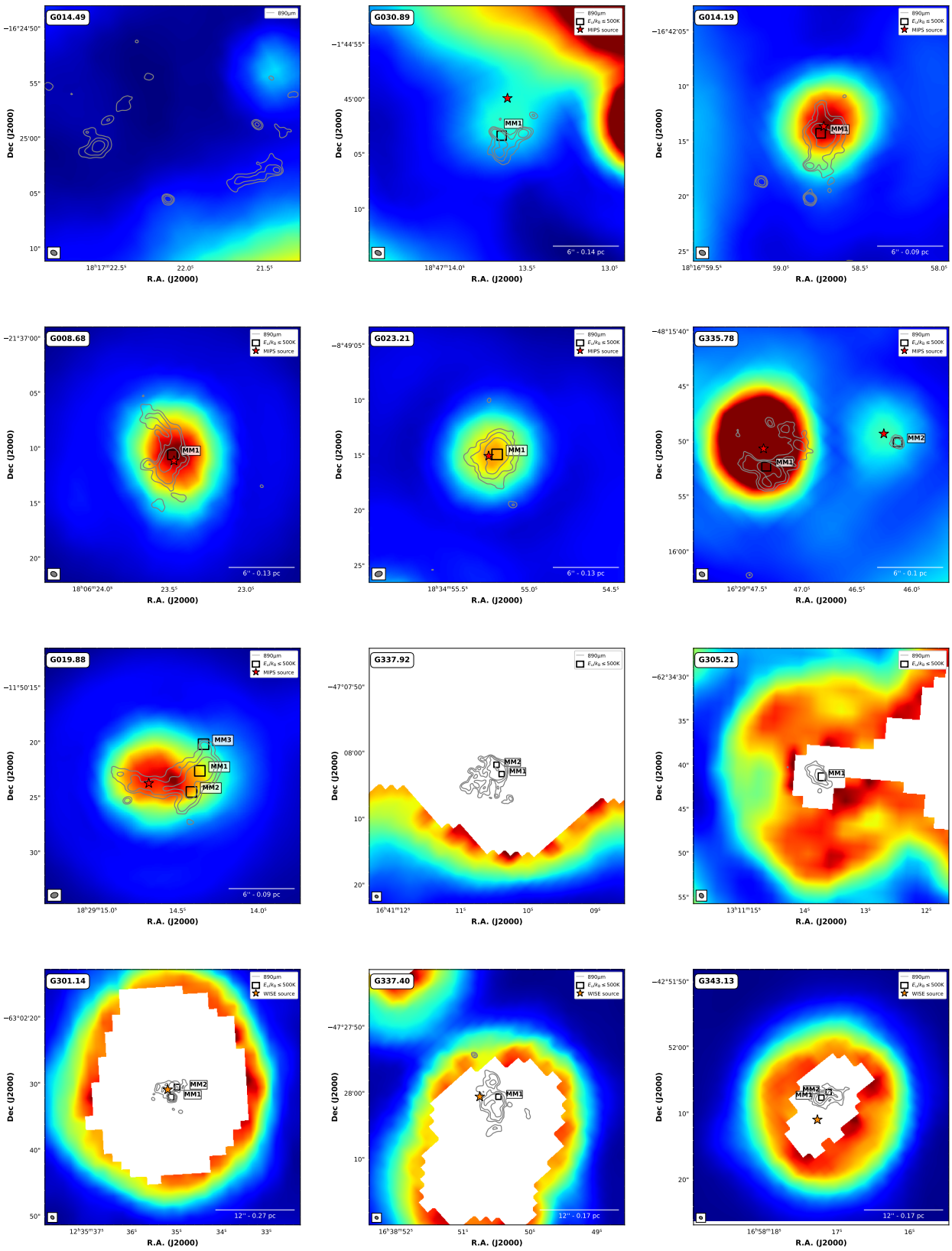

Fig. C.1. Panel showing the 24 μm MIPS images (background) of all 12 sources in the sample. Silver contours show the continuum emission at [3, 5, 10]σ. The black squares indicate the names and the positions of $v_t \geq 1$ cores with low-$\Delta E/k_B$. For G014.49, the absence of lines contours and IR emission indicates a non-detection. The red star marks point sources in the MIPSGAL catalog (Gutermuth & Heyer 2015), with exceptions for G030.89 and secondary sources in G335.78, where MIPS centroids are determined in this work. The orange stars indicate the WISE catalog centroid (Cutri et al. 2012) for saturated MIPS sources: G337.92, G301.14, G337.40, and G343.13. The absence of stars (e.g., G305.21, G337.92) indicates complex, diffuse emission not in the catalogs. The ALMA beam size (~0.6″) is shown in the bottom-left corner, while the MIPSGAL (~6″) or the WISE (~12″) beam size is in the bottom-right.